The Tender Energy Spectroscopy Beamline at SSRF*

Shu-Min Yang,[1] Ling-Ling Guo,[1] Bing Nan,[1] Ying Zhao,[1] Yan-Qing Wu,[1, †] Zhi Guo,[1] Chen Tian,[1] Bo Zhao,[1] Chao-Fan Xue,[1] Jun Zhao,[1] Shuang Song,[1,2] Zhen-Ye Liang,[1,2] Li-Na Li,[1] Yong Wang,[1, ‡] and Ren-Zhong Tai[1, §]

[1]*Shanghai Advanced Research Institute, Chinese Academy of Sciences, Shanghai 201204, China*
[2]*University of Chinese Academy of Sciences, Beijing 100049, China*

The tender energy spectroscopy beamline (BL16U1) is one of the phase-II beamline at the Shanghai Synchrotron Radiation Facility (SSRF). The design and performance of the tender energy spectroscopy beamline at SSRF are described in this paper. Based on a 26 mm-period in vacuum undulator (IVU) source, the beamline is to give an operable energy range between 2.1 and 16 keV, covering the K-edges of those elements from P to Rb and the L_3-edges of those elements from Zr to Bi. The principal optical elements of the beamline consist of a toroidal mirror, a liquid-nitrogen cooled double-crystal monochromator, a high harmonic rejection mirror and two pairs of Kirkpatrick–Baez (KB) mirrors. Three end-stations, including the non-focusing, microprobe and sub-microprobe end-stations, are installed on the beamline. X-ray fluorescence (XRF), X-ray absorption spectroscopy (XAS) including X-ray absorption near-edge structure (XANES) and extended X-ray absorption fine-structure (EXAFS), have been achieved under vacuum or He atmosphere at the non-focusing end-station with a spot size of $\sim 670 \times 710\ \mu m^2$. Based on two KB mirrors systems, micro-X-ray fluorescence (µXRF) mapping and micro-X-ray absorption near-edge structure (µXANES) studies will be operated with a spot size of nearly $\sim 3.3 \times 1.3\ \mu m^2$ at the microprobe end-station, and with a smaller spot size of $\sim 0.5 \times 0.25\ \mu m^2$ at the sub-microprobe end-station. Up to now, the non-focusing end-station of BL16U1 beamline is officially opened to users in Jan. 2024. The microprobe and sub-microprobe end-stations will be opened to users in the near future. This paper describes the characteristics, short-term technical developments and a few of the early experimental results of this new beamline.

Keywords: Tender energy X-ray spectroscopy, X-ray fluorescence, SSRF, X-ray absorption spectroscopy (XAS), Microprobe

I. INTRODUCTION

As the first third-generation synchrotron radiation light source in the main land of China, Shanghai Synchrotron Radiation Facility is equipped with a storage ring energy of 3.5 GeV, a circumference of 432 m and an emittance around 3.9 nm rad [1]. SSRF opened to users in 2009 with 7 Phase-I beamlines [2]. Over the next few years, 6 other beamlines were built as part of the Follow-up Beamline Program (FBP). Within the framework of SSRF Phase-II Beamline Project (2016) [3, 4], 16 new beamlines and more than 30 end-stations have been built. The photon energy extends to previous uncovered regions such as the tender x-ray region (BL16U1), the super-hard x-ray region [5] and the low-energy gamma-ray region [6].

XAS techniques, including XANES and EXAFS, have been recognized as efficient and comprehensive analytical tools for probing the electronic and local atomic structure order of metals/elements due to its advantages of element selectivity, valence state identification, and characterization of local atomic structure. Up to now, XAS platforms, including the soft X-ray spectromicroscopy beamline (BL08U1A, STXM, 250-2000 eV, [7]), the X-ray absorption fine structure beamline (BL14W1, XAFS, 4.5-50 keV, [8]), the hard X-ray micro-focusing beamline (BL15U1, 5-20 keV, [9]) and the hard X-ray spectroscopy beamline (BL11B, 5-30 keV, [10]) et al., can be supported to users from soft X-ray to hard X-ray in SSRF.

Thanks to the SSRF Phase-II Beamline Project, the tender-energy spectroscopy beamline (BL16U1) is the only one beamline designed to fulfill the tender photon energy gap in SSRF. The tender energy range of 2 to 5 keV, between the energy ranges of soft and hard X-rays, covers the K-edges of those elements such as phosphorus (P), sulfur (S), chlorine (Cl), potassium (K), calcium (Ca) and titanium (Ti) et al., which are important elements in soil and environmental sciences [11–17], geologic and cosmologic materials [18–20], life sciences [21–23], catalysis and archaeology sciences [24, 25]. The tender energy range of 2 to 5 keV also covers the L-edges of Mo to I, which are important elements for novel materials [26], mineral resources [27], environmental contaminants and biological toxins [28]. There are several beamlines in the world which foucus on the tender X-ray energy region, including the Diamond-I18 (2-20.7 keV) [29], SLS-PhoenixI (0.8-8 keV) [30], CLS–SXRMB (1.7-10 keV) [31], ESRF-ID21 (2-10 keV) [32], 8-BM at NSLS-II (2-5.5 keV) [33], the BL27SU at SPring8 (2.1-3.3 keV) [34], the 4B7A at BSRF (1.75-6.0 keV) [35] and the TPS 32A at NSRRC [36] (1.7-11 keV) etc. Among all these beamlines, XAS and XRF imaging with microprobe are their main research methods.

Taking advantage of the high brightness of SSRF, BL16U1 beamline is designed to cover the X-ray energy range of 2.1-16 keV by using an U26 in-vacuum undulator (IVU). Besides tender X-ray energy range, the energy range of the BL16U1 beamline also covers most of the transition metals, non-metallic elements, especially in the field of energy, catalysis

* Supported by the National Key R & D Program of China (Grant No.2021YFA1601003 and the financial support of the SSRF Phase-II project). We also thank those staffs in the department of beam engineering technology in SSRF for their helping in beamline design and installation.

† Corresponding author, wuyanqing@sari.ac.cn
‡ Corresponding author, wangyong@sari.ac.cn
§ Corresponding author, tairz@sari.ac.cn

and other areas of concern, such as titanium (Ti), nickel (Ni), iron (Fe), gold (Au), platinum (Pt), palladium (Pd), etc. Based on a toroidal mirror, a liquid-nitrogen cooled double-crystal monochromator and a high harmonic rejection mirror, XAS can be obtained at the non-focusing end-station with a spot size of $\sim 670 \times 710\ \mu m^2$. The samples can be operated under vacuum (lower than 1 mbar). But if samples are aqueous, Helium gas will be purged into the vessel and no vacuum is used. Based on two pairs of KB mirrors, XANES and XRF mapping will be operated at the microprobe end-station with a spot size of nearly $\sim 3.3 \times 1.3\ \mu m^2$, and at the sub-microprobe end-station with a smaller spot size of $\sim 0.5 \times 0.25\ \mu m^2$. The BL16U1 beamline construction was finished in Jul. 2023 and the non-focusing end-station has been officially opened to users since Jan. 2024. The microprobe and sub-microprobe end-stations will be opened to users in the near future. The beamline design, its short-term technical developments and a few of the early experimental results are described in this paper.

II. BEAMLINE

Specific optimizations of beamline design have been conducted to meet the requirement of flux and focusing of the beamline. An undulator sorce is used to get the high flux density in small spot sizes for microprobe XRF imaging. High-angular-range monochromator design are needed for the low critical energy of 2.1 keV. Harmonic rejection mirrors with different incident angles are used for different energy-ranges, and different coatings are required to avoid the absorption edges from the mirrors coating. According to the property of users samples, vacuum or He atmosphere can be opened to users.

A. Light source

The up-stream of a 12 m long canted long straight section in SSRF is selected as the light source for the tender energy spectroscopy beamline, and the down-stream one (3.06 m long) is used for the fast X-ray imaging beamline (BL16U2) [37, 38]. An U26 in-vacuum undulator (IVU) with 3.2 m length, 26 mm period and 6 mm minimum gap was finally chosen as the light source. Detailed information for the undulator of BL16U1 beamline is shown in Table. 1. The maximum magnetic field strength exceeds 1.02 T with a total power of over 7.7 kW. By tuning its gap from 6 to 15 mm, 1–7$^{\mathrm{th}}$ harmonics, and X-ray energy ranges between 2.1–16 keV can be generated.

Synchrotron radiation from an undulator source (planar mode) has high brilliance and narrow spectral range which is too narrow to be used in EXAFS experiments. The EXAFS technique requires high photon flux and a spectral range nearly 1000 eV. For the IVU design, taper mode are usually used to expands the bandwidth of the undulator source for EXAFS detection [39]. Taper mode means the two out-vacuum girders are tilted. In BL16U1, with the maximum gap taper adjustment range of 0.5 mm, which means a reproducible mechanical gap difference between exit gap and entrance gap (± 0.5 mm [40]), EXAFS above 5 keV can be obtained. In SSRF, "Taper mode" is also used by the BL15U beamline [9]. However, the taper mode widens the spectrum at the expense of reducing the brilliance of the undulator [39]. Now we use taper mode at the non-focusing end-station for EXAFS detection and use planar mode (Taper=0) at the microprobe and sub-microprobe end-stations for focusing. The gap-scan mode, in which the gaps of IVU are adjusted according to the energy, will be used in the future.

TABLE 1. Main characteristics of the U26 in-vacuum undulator.

Period (mm)	26
Length (m)	3.2
Number of periods	123
Maximum magnet field (T)	1.02
Minimum gap (mm)	6
Maximum k value	2.48
Fundamental energy (keV)	1.1-3.3
Maximum power (kw)	7.7

B. Beamline optics

The main optical layout of the beamline is shown in Fig. 1. A toroidal mirror, a liquid-nitrogen cooled double-crystal monochromator, a high harmonic rejection mirror and two pairs of Kirkpatrick–Baez mirrors are installed on the beamline. Details on all beamline mirrors are listed in Table. 2. The layout of the beamline is similar to that of the hard X-ray micro-focusing beamline (BL15U1) at SSRF [9] and the microfocus spectroscopy beamline (I18) at Diaomnd light source [29]. A horizontally deflecting toroidal mirror (FMB Oxford) achieved by mechanically bending a sagittal cylindrical mirror is placed at 35 m from the source. A set of water-cooled slits (Slit1, Fig. 1), 26 m from the source, are used to define the incoming beam on the toroidal mirror. By considering the effective length, reflectivity and heat load, the toroidal mirror is water-cooled and operates at a grazing incidence angle of 3.5 mrad with an active area of 800 mm. Rh coating on single crystal Si substrate is designed for high energies above 8 keV and Si coating is designed for the photon energy below 8 keV. The two coatings can be switched by an in-vacuum translation mechanism. Usually, for simplifying the beamline adjustment, only Rh coating is used for the whole energy range, 2.1-16 keV. By using the toroidal mirror, the beam in vertical plane will be collimated and the influence of vertical source divergence will be removed. Thus, the energy resolution is primarily a function of the bandpass of the crystals used in the monochromator. In horizontal plane, the beam is focused using an mechanically elliptical bend onto the secondary source. The secondary source is placed 48 m away from the light source, where the secondary slits (MS1 in Fig. 1, 10 m after the monochromator) is installed. The secondary source will be used for the horizontal focusing optics of the

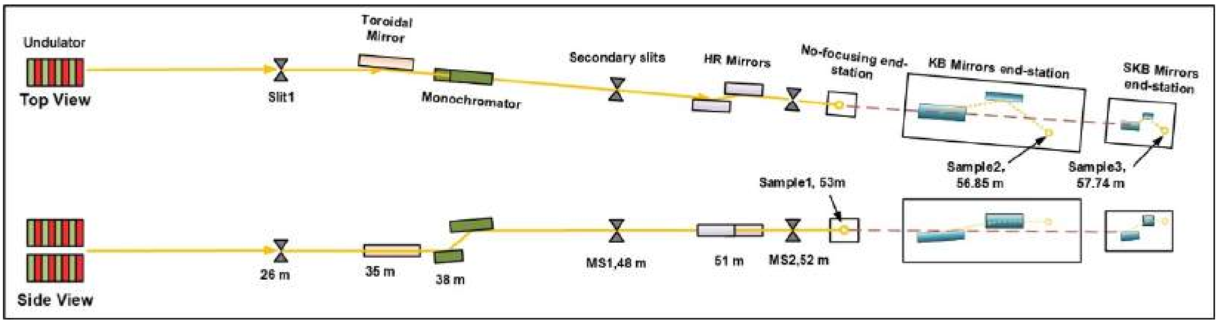

Fig. 1. (Color online) Schematic showing of the principal elements of the beamline.

TABLE 2. Main specifications of the BL16U1 beamline Mirrors.

	Toroidal Mirror	**Harmonic rejection Mirror**	**KB Mirror**	**SKB Mirror**
Type	Cylinder with bender	Flat	(Fixed surface) shape Parabolic for VFM Elliptical for HFM	(Fixed surface shape) Parabolic for VFM Elliptical for HFM
Size	800 mm length 25 mm wide	280 mm length 25 mm wide	22 mm wide 300 mm length for VFM 340 mm length for HFM	18 mm wide 70 mm length for VFM 40 mm length for HFM
Mirror material	Silicon	Silicon	Silicon	Silicon
Optical quality	Sagittal radius 0.245 m Meridional radius 5.417 km 0.3 nm roughness	Sagittal slope error 10 μrad 0.3 nm roughness	Sagittal slope error 10 μrad 0.3 nm roughness	Sagittal slope error 5 μrad 0.3 nm roughness
Grazing angle	3.5 mrad	Cr, 2.05-3.5 keV, 10 mrad Si, 3.5-7.5 keV, 3.5 mrad Rh, 7.5-13 keV, 3.5 mrad	4 mrad for VFM 4.7 mrad for HFM	4 mrad for VFM 4.7 mrad for HFM
Coatings	Rh with 10 mm wide Si with 10 mm wide	Cr with 5 mm wide Si with 5 mm wide Rh with 5 mm wide	Ni with 6 mm wide Si with 6 mm wide Rh with 6 mm wide	Ni with 5 mm wide Si with 5 mm wide Rh with 5 mm wide
Coatings translation	in vacuum	in vacuum	in vacuum	in vacuum
Distance from source	35 m	51 m	56.85 m (focal spot)	57.74 m (focal spot)
Manufacturer	FMB Oxford	TOYAMA	JTEC	JTEC

KB mirrors after the monochromator.

Owing to the high-power density of the undulator, the monochromator is installed after the toroidal mirror. A fixed-exit double-crystal monochromator (DCM, TOYAMA) is located about 38 m away from the light source. Photon energies between 2.1-16 keV with resolution below 1.64×10^{-4} ($\Delta \mathrm{E}/\mathrm{E}@2.5\ \mathrm{keV}$) can be obtained with Si (111) crystal sets. The Si (220) crystal is applied for a better energy resolution with photon energies between 3.35-16 keV. The crystals are translated by an in-vacuum translation mechanism. Owing to the high power density of the undulator source, the first and second crystals are indirectly cooled with liquid nitrogen. The fixed beam exit is maintained by translating the second crystal vertically. The final height difference is chosen as 25 mm. In order to cover the required energy range, the monochromator has an high angular range of 0-75°. To maintain the alignment of the first and second crystal lattice planes over this angular range, two coarse motors, $\pm 12\ \mathrm{mrad}$ and $\pm 8\ \mathrm{mrad}$, are used for the roll and pitch coarse adjustment, and two piezo actuator ($\pm 0.2\ \mathrm{mrad}$) are also used for the fine adjustment of the roll and pitch motors.

Two sets of monochromatic four knife slits without water cooling are installed downstream of the monochromator. The layout of the beamline slit is similar to that of the microfocus spectroscopy beamline (I18) at Diaomnd light source [29]. The first monochromatic four knife slit (MS1, Fig. 1), 10 m away from the monochromator, serves as the secondary source for the focusing optics in the horizontal direction. At this point the biggest slit size is $350 \times 1400\ \mu\mathrm{m}^2$ (h×v). Another monochromatic four knife slit (MS2, Fig. 1), 4 m away from MS1, is used to remove the scatter of the beam at non-focusing end-station and limit the horizontal and vertical beam size onto the KB and SKB mirrors. At this point the biggest slit size is $1600 \times 1400\ \mu\mathrm{m}^2$ (h×v). The slit position is fixed but the slit size can be controlled via a parallelogram mechanism. The slit size can be changed according to different spot size at three end-stations.

A harmonic rejection mirror (HRM,TOYAMA) is placed at 51 m form the source. A pair of horizontally reflecting flat silicon mirrors is used for rejection of the higher harmonics. The mirrors have three stripes of chrome (Cr), silicon (Si)

and rhodium (Rh), which are translated in vacuum vertically. The Cr reflector can be used for 2.05-3.5 keV with a grazing incidence angle of 10 mrad. The Si reflector can be used for 3.5-7.5 keV with a grazing incidence angle of 3.5 mrad. The Rh reflector can be used for 7.5-13 keV with a grazing incidence angle of 3.5 mrad. The grazing incidence angle is regulated by two horizontal vacuum motors installed up and down stream of the mirror. Besides the three coatings which reflect the x-ray beam, the mirrors can be moved out of the beam in vacuum translation to make sure the incoming x-ray go through without being reflected. In our beamline, due to the use of Rh coating in the toroidal mirror, the HR mirrors are usually moved out of the beam for the energy above 8 keV.

III. EXPERIMENTAL STATION

Aimed at XAS and XRF microprobe imaging between 2.1-16 kev, three end-stations are installed on BL16U1 beamline, which are the non-focusing end-station, the microprobe and sub-microprobe end-stations focused by two sets of KB mirrors. The schematic layout of the three end-stations is shown in Fig. 2. The specifications of energy range, energy resolution, flux and spot size at different end-stations are listed in Table. 3.

The non-focusing end-station is placed after the harmonic rejection mirror, about 53 m away from the source. X-ray fluorescence (XRF) and X-ray absorption spectroscopy (XAS) including X-ray absorption near-edge structure (XANES) and extended X-ray absorption fine-structure (EXAFS) can be achieved with a spot size of $\sim 670 \times 710\ \mu\mathrm{m}^2$. After the non-focusing end-station, two sets of K-B systems (Motors from CINEL, Mirrors from JTEC) are chosen as the microprobe and sub-microprobe tools to focus the secondary source to a spot with micron size (Sample 2) and a spot with sub-micron size (Sample 3) in two different vacuum vessels, Fig. 2. Two vacuum valves (V1 and V2 in Fig. 2) are installed downstream the non-focusing end-station. The valves are used when He atomephere is used in the non-focusing end-station. Liquid in-situ end-station will be installed in the future by removing the vacuum tube between V1 and V2 and a Be window will be installed after V1 valve to maintain the vacuum of the non-focusing vessel.

The photons flux and energy resolution of the beamline are obtained at the non-focusing end-station. Fig. 3(a) shows the photons flux of the beamline measured at I_1 in the non-focusing end-station. The designed spot size (full width at half maximum, FWHM) at this station is $\sim 670 \times 710\ \mu\mathrm{m}^2$. The photons flux of the beamline at this station is above 2.0×10^{12} photons/s for the energy between 2.15 to 13 keV. And it is between 1.5×10^{12} to 5.0×10^{11} photons/s for the energy between 14 to 16 keV. We don't think it is the best status of our beamline now. Better flux value should be obtained by longer use. Fig. 3(b) shows the rocking curve of 2.5 keV by using a Si (111) single crystal. The DCM energy was set to 2.5 keV and a Si (111) single crystal is put after the non-focusing end-station and roated in vacuum around $52.2669°$. A photodiode (AXUV300C) was used to get the diffraction photons flux from the Si (111) single crystal. The FWHM ($\Delta\theta$) of the rocking curve at 2.5 keV is $\sim$ 212 μrad, an energy resolution of $\sim 1.64 \times 10^{-4}$ is obtained by $\Delta\theta/\tan\theta$, where θ is the diffraction angle of Si (111) at 2.5 keV, $52.2669°$.

Micro-X-ray fluorescence (μXRF), micro-X-ray fluorescence mapping and micro- X-ray absorption near-edge structure (μXANES) can be obtained at the KB and SKB microprobe end-stations in the near future. Details of KB and SKB mirrors are listed in Table. 2. For each set of KB mirrors, fixed surface shape KB mirrors are used. The mirror substrates are made of silicon and coated with Ni, Si and Rh stripes. The coating stripes are translated by an in-vacuum translation mechanism. A vertically focusing mirror (VFM) and a horizontally focusing mirror (HFM) are aligned behind each other in orthogonal planes. The incident angles are 4 mrad and 4.7 mrad for VFM and HFM mirrors, respectively.

A. Non-focusing end-station

The non-focusing end-station is housed in a vacuum vessel allowing operation in vacuum (1-10^{-6} mbar) or He atmosphere. No loadlock system is used for sample replacement in the non-foucusing end-staton. Usually, only the dry pump is turned on and a vacuum of 1 mabr is enough for the non-focusing end-station. He gas is purged into the vessel when there is water in the samples and no vacuum is used. The dry pump and turbo pump (Pfeiffer, HiPace 700) are turned on when high vacuum and KB systems are used. 20-30 mins are need for vacuum vent and samples replacement.

Fig. 4 shows the photograph of non-focusing end-station. A set of translation (X-Z) and rotation (R) motors (VACGEN) are used to adjust the sample position in the vacuum vessel. The sample holder is 9 cm in total length with a YAG crystal on the top to assist with beam location (inset in Fig. 4). Samples are usually smeared onto carbon or kapton tapes or pressed into disks. Usually, 6-9 samples can be put onto the sample holder at a time. By indirectly cooling with liquid nitrogen, the sample in the non-focusing end-station can be operated in vacuum under cryogenic conditions to $\sim$ 120 K. A graphene carbon window (Ketek, $\sim$900 nm thickness and $\sim$10 mm diameter) separates vacuum of the non-focusing vessel from the beamline. Four pieces of photodiodes (AXUV300C) are installed at the four corners of a 5 mm hole to measure the fluorescence after a thin Al film with 2 μm thickness, which is used as the incident beam intensity (I_0). Due to the tight space of the beamline, the I_0 detector are placed before the graphene carbon window. Before the I_0 detector, several Al foils with different thickness (25-500 μm) are used for the attenuators. A photodiode (AXUV300C) is mounted after the sample in the vacuum vessel to measure the transmitted beam intensity (I_1). The I_1 photodiode can be moved out of the beamline in vacuum translation when the KB microprobe end-station is used. A three-channel silicon drift diode (SDD, RaySpec) with a collimated active area of 150 mm^2 is installed perpendicularly to the beamline for

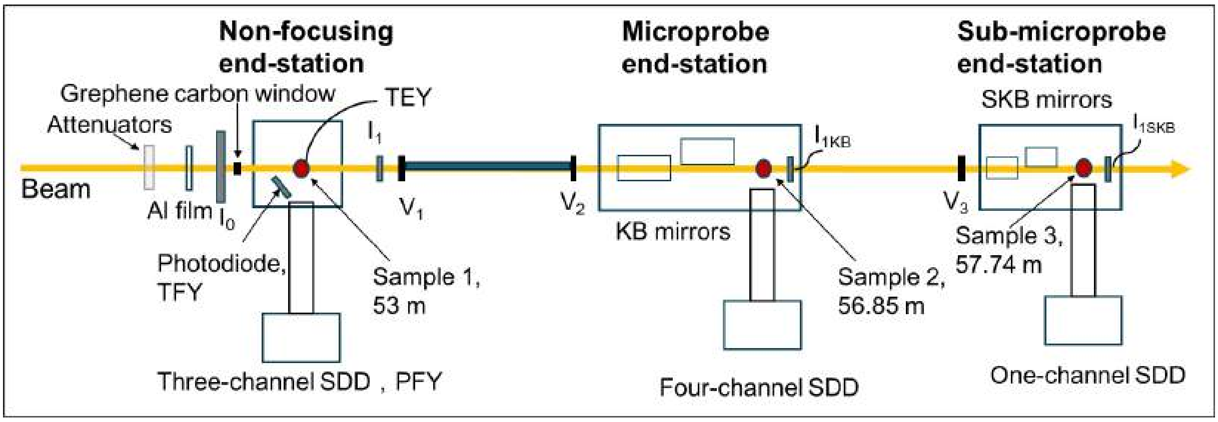

Fig. 2. (Color online) The schematic layout of the experimental end-stations at BL16U1.

TABLE 3. Specifications of energy range, energy resolution, flux and spot size at different end-stations.

End-station	**Non-focusing**	**Micorprobe**	**Sub-microprobe**
Energy range	2.1-16 keV	2.1-16 keV	2.1-16 keV
Energy resolution @2.5keV@Si(111)	1.64×10^{-4}	1.64×10^{-4}	1.64×10^{-4}
Flux (photons/s)	>2.0×10^{12}@2.15-13 keV >5.0×10^{11}@14-16 keV	2.48×10^{12}@10 keV	7×10^{10}@2.5 keV
Spot size (FWHM, h × v)	670×710 μm^2	$\sim 3 \times 1.3$ μm^2	$\sim 0.5 \times 0.25$ μm^2

XRF detection and partial fluorescence yield (PFY) detection of the sample. A photodiode is installed next to the SDD to measure the total fluorescence yield (TFY) of the sample. Total electron yield (TEY) mode is also used to measure the sample current. The schematic of three detection modes is shown in Fig. 2.

Here we show several XAS results done at the non-focusing end-station, Fig. 5. According to the morphology, conductivity and absorption edge of samples, different XAS detection modes are used. For elements with absorption edge above 5 keV, TFY, PFY and transmission modes are used for XAS detection according to its morphology and concentration. And for elements with absorption edge below 5 keV, TEY, TFY and PFY modes are used. For PFY mode with low concentration and transmission mode with high concentration, samples should be pressed into disks with proper thickness. And for TEY and TFY modes, samples usually should be smeared onto carbon or kapton tapes. The I_0 and I_1 photodiodes in Fig. 4 are used for the transmission mode. The P K-edge XANES of KH_2PO_4 done by TEY mode is shown in Fig. 5(a). The P K-edge XANES is very similar to that done at ESRF-ID21 [41]. The max of "white-line" (s→ p electronic transition) of P K-edge of KH_2PO_4 is corrected to 2152.8 eV according to ID21 [41]. And Sr K-edge XANES of $C_4H_6O_4Sr$ done by transmission mode is shown in Fig. 5(b), the spectrum is similar to the XANES spectrum of $SrCO_3$ in [42]. The test results show that the photon energy range of the beamline covers the design energy range between 2.1 and 16 keV. During the test, each energy integral time is one second with different undulator gap. The undulator tapper is set as 0.45 mm and the beam current is 220 mA.

The S K-edge XANES of $CaSO_4$ done by TFY, TEY and PFY modes are shown in Fig. 5(c). The S K-edge XANES is very similar to that done at ESRF-ID21 [43]. The max of "white-line" (s→ p electronic transition) of S K-edge of $CaSO_4$ is corrected to 2482.5 eV according to ID21 [43]. High purity $CaSO_4$ powder and $CaSO_4$ powder diluted by LiF to a mass concentration of 2.5% and 0.5% were used as the samples. The $CaSO_4$ powder was smeared evenly onto the kapton or carbon tapes with very thin thickness. High purity $CaSO_4$ powders done by TEY and TFY modes are shown in Fig. 5(c). Due to the self-absorption of fluorescence, the fluorescence spectral signal intensity of TFY (red) is much lower than that of TEY mode (blue) for sample with high purity. In Fig. 5(c), $CaSO_4$ with 0.5% was done by PFY mode (green) and $CaSO_4$ with 2.5% concentration was done by TFY mode (purple). The order of normalized maximum values are 100% TEY mode, 0.5% PFY mode, 2.5% TFY mode and 100% TFY mode, respectively. Usually, TEY is used for samples with high concentration, TFY is used for samples with concentrations between 1% and 5%, and PFY is used for samples with concentrations less than 1% [35]. $CaSO_4$ with 0.5% was done by TFY mode with very close working diatance between sample and TFY photodiode ($\sim$ 10 mm distance), the spectrum is not so smooth. Thus,

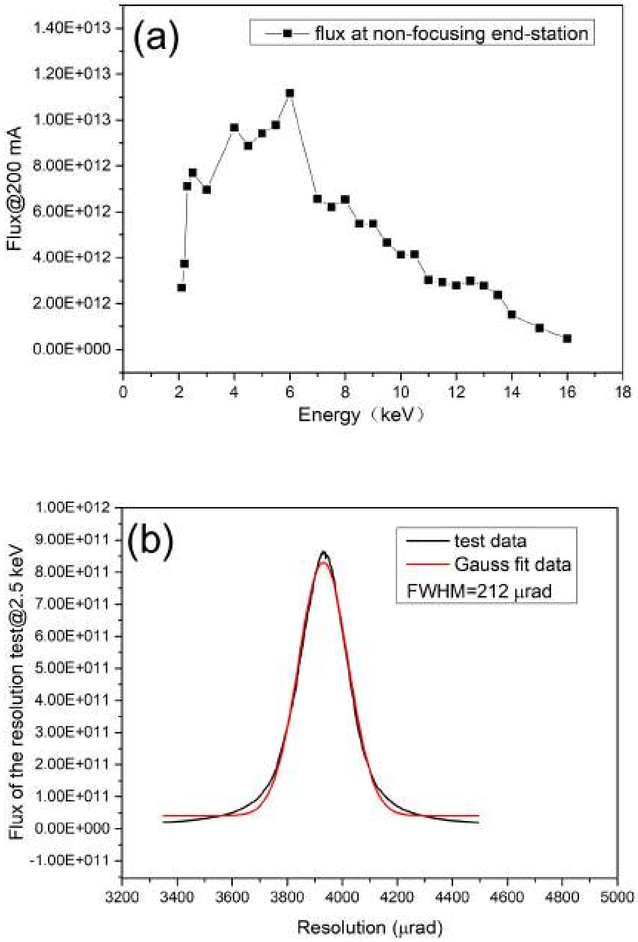

Fig. 3. (Color online) Flux and rocking curve obtained at the non-focusing end-station. (a) Flux obtained at the non-focusing end-station at 200 mA. (b) Rocking curve obtained after the non-focusing end-station at 200 mA and 2.5 keV.

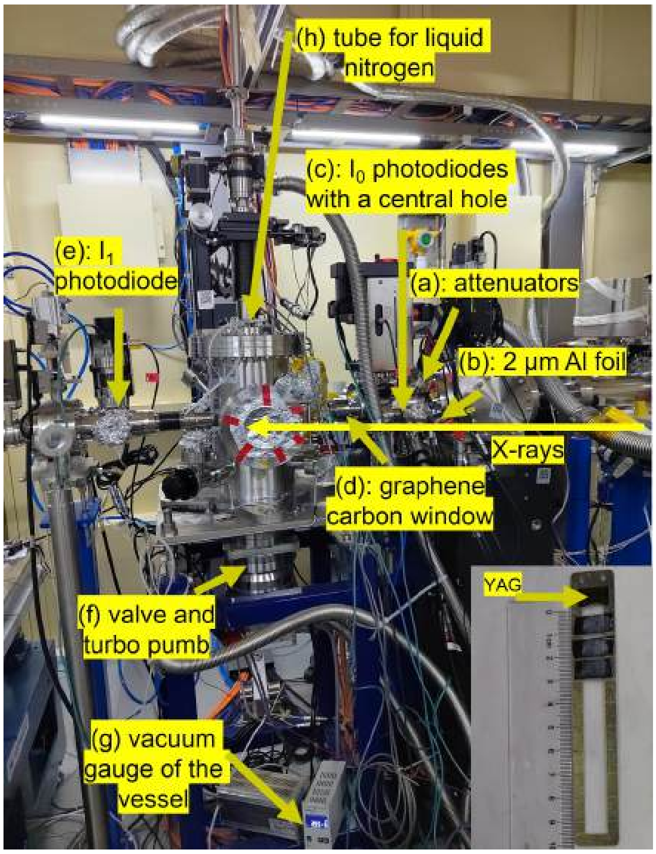

Fig. 4. (Color online) Photograph of the non-focusing end-station. (a) attenuators used by several Al foils with thickness from 25 to 500 μm, (b) Al foil for I_0 with thickness of 2 μm, (c) the I_0 detector by four photodiodes with a 5 mm pinhole, (d) graphene carbon window, (e) the I_1 detector, a normal photodiode, (f) valve and turbo pump for the vessel, (g) vacuum gauge of the vessel, (h) the tube for liquid nitrogen.

for samples with low concentration ($< 1\%$), PFY mode is suggested.

The results of K-edge XAFS of Ni standard foil done by transmission mode is shown in Fig. 5(d). The I_0 and I_1 photodiodes in Fig. 3 were used for the transmission mode. The EXAFS $k^2\chi$ data and Fourier transform (FT) spectra of Ni standard foil K-edge XAFS spectrum are shown in Fig. 5(e) and Fig. 5(f). For energy calibration, the energy and brag angle of the DCM are reset according to the first derivative spectrum of Ni Foil from Exafs Materials [44]. After energy calibration, the EXAFS $k^2\chi$ data and Fourier transform (FT) spectra of Ni standard foil K-edge XAFS spectrum can be compared to that done at X18B at the National Synchrotron Light Source [45]. The K-edge XAFS of Ti standard foil done by transmission mode is shown in Fig. 5(g). The I_0 and I_1 photodiodes in Fig. 4 were used for the transmission mode, too. For comparison, K-edge XAFS spectrum of TiO_2-nano (rutile) diluted with LiF to a mass concentration of 3% was also tested by the TFY mode, Fig. 5(g). The energy is also calibrated according to the spectrum of Ti Foil from Exafs Materials. The EXAFS $k^2\chi$ data and Fourier transform (FT) spectra of Ti standard foil and TiO_2-nano (rutile) are shown in Fig. 5(h) and Fig. 5(i). The EXAFS $k^2\chi$ data and Fourier transform (FT) spectra of Ti standard foil K-edge XAFS spectrum can be compared to that done at TPS 44A at Taiwan Photon Source [46]. The EXAFS and Fourier transform (FT) spectra of TiO_2-nano (rutile) are similar to that obtained in the synchrotron laboratory HASYLAB/DESY, Hamburg [47].

These figures demonstrate that the BL16U1 can collect XAS spectrum across the whole target photon energies range, 2.1-16 keV. For the tender energy range of 2 to 5 keV, XANES spectra for phosphorus (P), sulfur (S), chlorine (Cl), potassium (K), calcium (Ca) et al. were usually collected by TEY, TFY and PFY modes. For the energy above 5 keV, XAFS spectra were usually collected by transmission, TFY and PFY modes. Though ion chamber is mainly used for synchrotron spectroscopy beamline in the world, our results show that photodiode can also be used by XANES and XAFS spectrum. The only drawback of photodiode is the diffraction peaks resulting from the crystalline nature of photodiodes

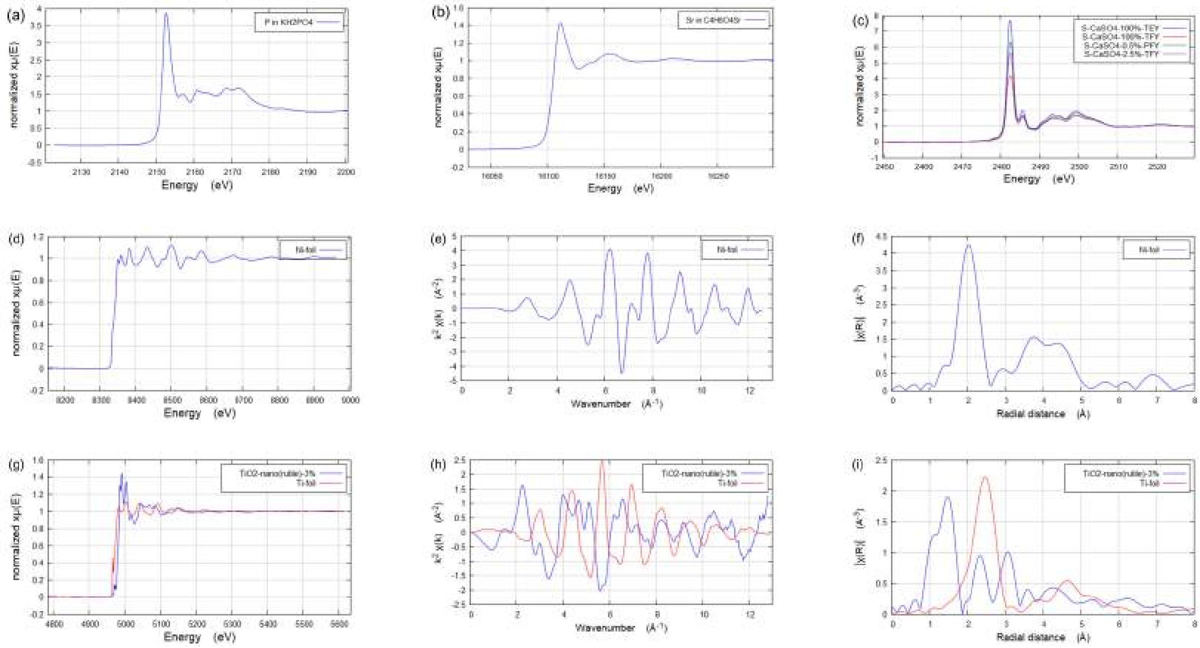

Fig. 5. (Color online) (a) The normalized P K-edge XANES of KH_2PO_4 done by TEY mode, (b) The normalized Sr K-edge XANES of $C_4H_6O_4Sr$ done by transmission mode, (c) The normalized S K-edge XANES of $CaSO_4$ with different concentration done by TFY, TEY and PFY modes, (d) The normalized K-edge XAFS of Ni stand foil done by transmission mode, (e) the EXAFS $k^2\chi$ data and (f) the Fourier transform (FT) spectra of Ni standard foil, (g) The normalized K-edge XAFS of Ti stand foil done by transmission mode and TiO_2-nano (rutile) powder with a mass concentration of 3% done by TFY mode, (h) the EXAFS $k^2\chi$ data and (i) the Fourier transform (FT) spectra of Ti standard foil and TiO_2-nano (rutile) powder.

[48], which can be removed by the "deglitch" function in the Athena software.

Non-focusing end-station has been in operation for more than one year since the final acceptance test in July 2023. Up to now, this station has received more than 85 users with a total user time of 2086 hours. Important achievements have been made in many fields, especially in Co oxidation reaction [49], semi-hydrogenation of propylene [50] and flexible aqueous batteries [51] etc. This end-station is currently officially open to users.

B. Microprobe and sub-microrobe end-stations

Aimed at the analysis of materials at the microscopic scale, microprobe endstations have been constructed and built among the worldwide synchrontron facilities in recent years, Table. 4. A spot size of $\sim 2.1 \times 2.5$ μm^2 $(\mathrm{h} \times \mathrm{v})$ on Daimond I18 [29], a spot size of $\sim 2.5 \times 2.5$ μm^2 $(\mathrm{h} \times \mathrm{v})$ on SLS PHOENIX I [30], a spot size of $\sim 0.7 \times 0.35$ μm^2 $(\mathrm{h} \times \mathrm{v})$, or even smaller than 180 nm on ESRF ID21 [32], have been achieved by using the undulator source. By using a bending magnet source, the spot size in SXRMB beamline at CLS is nearly 10 μm [31] and the spot size in TES beamline at NSLS-II can be tuned from 2-25 μm [33]. For these microprobe beamlines, KB mirrors are used to focus the beam. Micro-X-ray fluorescence, micro-EXAFS and micro-X-ray diffraction are usually the main methods for these microprobe beamlines.

Here we focus on the micro-X-ray fluorescence and micro-XANES techniques. With the use of multi-channel silicon drift diode (SDD) detector, one can map the elemental distribution and correlations of elements on micrometre scale. With the micro-XANES scans, one can obtain the chemical speciation of elements, by recording XANES spectra of selected sample spots with grain sizes on the order of micrometer. Micro-X-ray fluorescence and micro-XANES can also be done on BL16U1 beamline at the microprobe and sub-microprobe end-stations by using two sets of KB-mirror systems. The microprobe and sub-microprobe end-stations are installed after the non-focus end-station. Two sets of KB mirrors are put in two different vacuum vessels, Fig. 6. The vacuum of the two sets of KB systems are lower than 5E-7 mbar by using ion pump, and two sets of loadloak systems are used for sample transfer.

1. *Microprobe end-station*

By using one pair of fixed surface shape KB mirrors, the focal spot of the microprobe end-station is about 56.85 m from the source. The mirror substrates are made of silicon and coated with 6 mm-wide Ni, Si and Rh stripes. The coating stripes are translated by an in-vacuum translation mechanism according to the energy. A vertically focusing mirror (VFM) and a horizontally focusing mirror (HFM) are aligned behind

TABLE 4. Main specifications of the TES beamline in the world.

Beamline name	Energy range	Spot size	Flux(photons/s)	Research methods
Diamond I18	2.05-20.7 keV	$2.1 \times 2.5\ \mu m^2$	3.5×10^{12}@8 keV	Micro-XRF, micro-EXAFS micro-XRD
SLS PhoenixI	0.8-8 keV	$2.5 \times 2.5\ \mu m^2$	1×10^{11}@400 mA	Micro imaging and XAFS
CLS SXRMB	1.7-10 keV	$1 \times 4\ mm^2$ $10 \times 10\ \mu m^2$	10^9-10^{11}@100 mA	XAS, XPS, XEOL Micro-XRF and XAFS
ESRF ID21	2-10 keV	$<180\ nm$ $\sim 0.8\ \mu m$ 300 to 50 μm	10^{10}-10^{11}	Micro and Nano XRF and XANES
NSLS-II 8-BM	2-5.5 keV	2-25 μm	Up to 10^{11}@500 mA	Microprobe XRF and EXAFS
SPring8 BL27SU	2.1-3.3 keV	$15 \times 15\ \mu m^2$	1×10^{11}@100 mA	Micro XANES and XRF
BSRF 4B7A	1.75-6.0 keV	$5 \times 3\ mm^2$	1×10^{11}@2.5 keV	XAS
NSRRC TPS 32A	1.7-11 keV	$0.3 \times 0.62\ mm^2$ $5 \times 5\ \mu m^2$	10^{12}@5 keV	XAS, XAFS, TXPS Micro XRF and XAFS

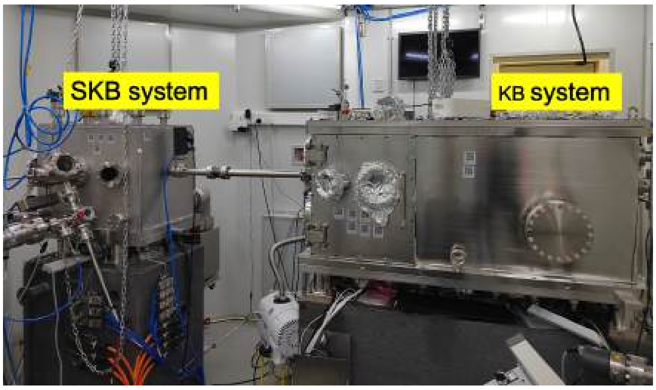

Fig. 6. (Color online) The vacuum vessels for KB abd SKB systems.

each other in orthogonal planes. The incident angles are 4 mrad and 4.7 mrad for VFM and HFM mirrors, respectively. Details of KB mirrors are listed in Table. 2.

For the first set of KB mirrors, the focal spot is located at 600 mm and 245 mm from the center of VFM and HFM mirrors, respectively, which gives a standard working distance of 75 mm from the end of the HFM mirror to the sample focal plane. A photograph of the KB mirrors and the sample stages is shown in Fig. 7(a). The mirrors and the sample holder are installed in the same vacuum vessel, without any vacuum window used for vacuum separation between the KB mirrors and the samples. A four-axis sample stage (Micronix) are used for sample positioning, Fig. 7(b). There is a 45° angle between the sample horizontal motion and the beam. The XYZ stages have a scanning precision accuracy of 200 nm. A photodiode (AXUV300C) is mounted after the sample in the vacuum vessel to measure the transmitted beam intensity (I_{1KB}).

To measure the focal spot size of the KB system, knife-edge scan using a 50 μm gold wire was used. The knife-edge scan is similar to that done by Ando et al. [52]. The beam profile was measured using a 50 μm gold wire that is scanned through the beam, with the intensity of the transmitted beam recorded by the photodiode (I_{1KB}) behind the gold wire. The smallest full width at half maximum (FWHM) of the spot size obtained at 10 keV is $4.59 \times 1.22\ \mu m^2$ ($h \times v$) , Fig. 7(c) and Fig. 7(d). Since there is a 45° angle between the sample horizontal motion and the beam, Fig. 7(b), the horizontal FWHM spot size is gotten by using the Gaussian fitting result to multiply sin (45°). Thus, the smallest FWHM of horizontal spot size at 10 keV is $3.25\ \mu m$. Considering the motor resolution, the focal spot size of the KB system should be $\sim 3.3 \times 1.3\ \mu m^2$ ($h \times v$). The photons flux at this station can be recorded by the photodiode (I_{1KB}). The highest current recorded by I_{1KB} is 3.5E-4 A@10 keV (Fig. 7(c) and Fig. 7(d)), the photons flux of the beamline at this station is above 2.48×10^{12} photons/s@10keV.

By using the same "I_0" mentioned in the non-focusing end-station, μXANES spectra and can be done in the KB vessel. A four-channel SDD (Vortex, Hitachi USA) with a collimated active area of 200 mm^2 is installed perpendicularly to the beamline for μXRF and PFY detection. Micro-XRF mapping can also be executed at the KB vessel. And because of the windowless design, micro X-ray fluorescence (μXRF) and micro X-ray absorption near-edge structure (μXANES) can only be achieved under vacuum at the microprobe end-station. Fig. 7(e) and Fig. 7(f) shows the μXRF mapping and μXANES of a Cu net. The type of Cu net is GILDER G200-C3. The scan range is $200 \times 200\ \mu m^2$ with a step size of 5 μm.

2. *Sub-microprobe end-station*

After the microprobe end-station, a pair of smaller KB (SKB) system is employed to focus the beam to a spot size with sub-micron level. When the X-ray is focused by the SKB system, the KB mirrors and photodiode in the microprobe end-station should be moved out of the beam in vacuum translation. The same as the KB system in the microprobe end-station, fixed surface shape SKB mirrors with Ni, Si and Rh stripes are also used in the SKB system. The coating stripes are translated by an in-vacuum translation mechanism. Details of SKB mirrors are listed in Table. 2.

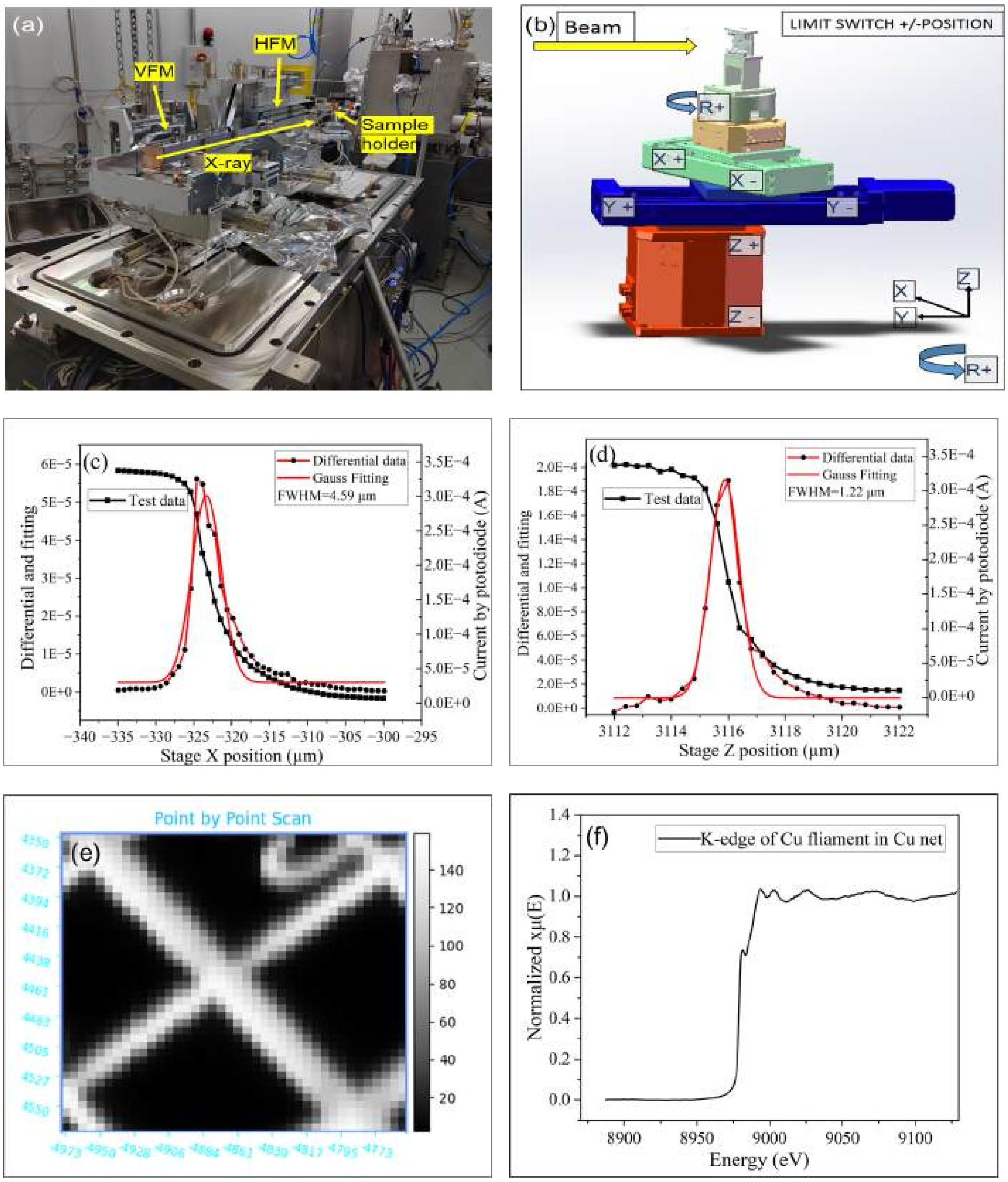

Fig. 7. (Color online) The photograph of KB mirror system (a) and the design view of sample stages (b), the horizontal with a 45° angle (c) and vertical (d) focused beam profiles of KB system at 10 keV. (e)The μXRF mapping and (f) μXANES of a Cu net.

For the SKB mirrors, the focal spot is located at 230 mm and 90 mm from the center of VFM and HFM mirrors, respectively, which gives a standard working distance of 60 mm from the end of HFM mirror to the sample focal plane. A design drawing of the SKB mirrors and the sample stages are shown in Fig. 8(a) and Fig. 8(b). Different from the KB system, the mirrors and sample holder are installed in different vacuum vessel, separated by a Be window (8 μm thickness and ∼9.2 mm diameter). For comparison with KB system, the SKB system has lower flux and smaller spot size. In-situ measurements under various conditions can be tested at this station. A four-axis sample stage (Micronix) are used for sample positioning. There is a 45° angle between the sample horizontal motion and the beam. The XYZ stages have a scanning precision accuracy of 50 nm. A photodiode (AXUV300C) is mounted after the sample in the vacuum vessel to measure the transmitted beam intensity (I_{1SKB}). With the same incident angles for VFM and HFM mirrors, a spot size of 0.67×0.21 μm^2 can be obtained at 2.5 keV by this SKB system, Fig. 8(c) and Fig. 8(d). A 45° angle between the sample horizontal motion and the beam is also used in the SKB sample stages, Fig. 8(b). And the horizontal FWHM spot size is obtained by using the Gaussian fitting result to multiply the sin (45°). Thus, the smallest FWHM of horizontal spot size at 2.5 keV is 0.47 μm. Considering the motor resolution, the focal spot size of the SKB system

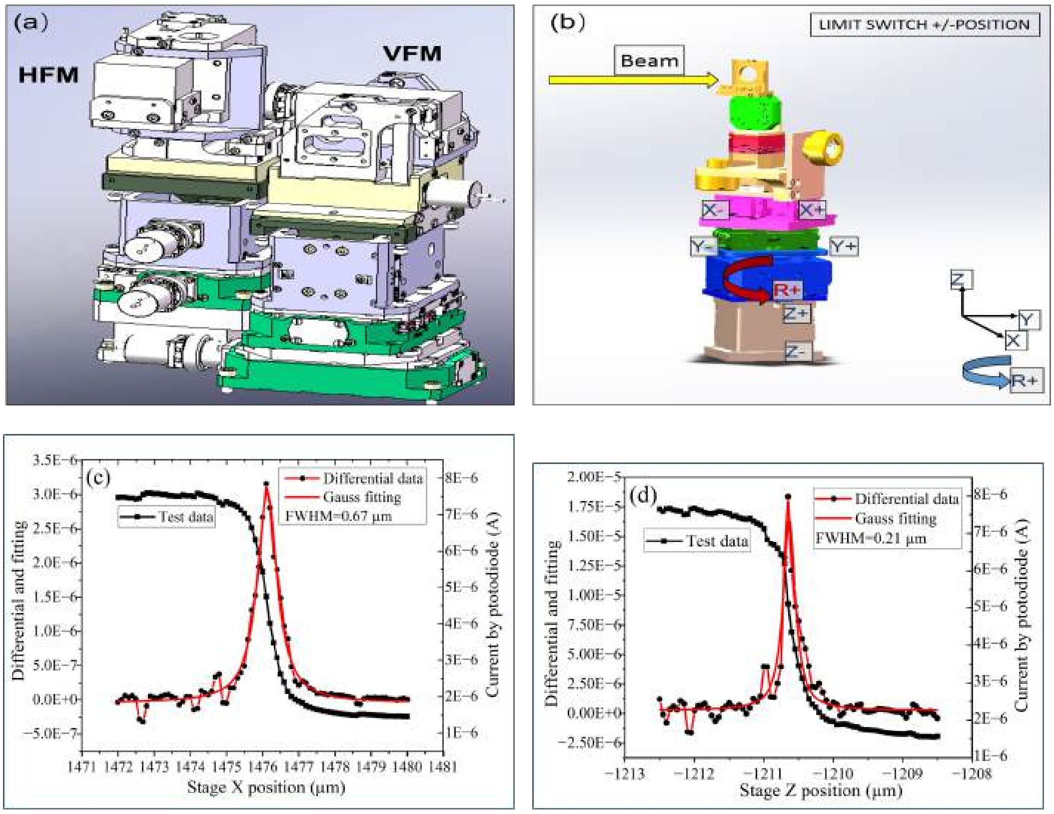

Fig. 8. (Color online) The design drawing of SKB mirror system (a) and the sample stages (b), the horizontal with a 45° angle (c) and vertical (d) focused beam profiles of SKB system at 2.5 keV.

should be $\sim\ 0.5 \times 0.25\ \mu\mathrm{m}^2$ (h × v). The photons flux at this station can be recorded by the photodiode ($\mathrm{I}_{1\mathrm{SKB}}$). The highest current recorded by $\mathrm{I}_{1\mathrm{SKB}}$ is 7.5E-6 A@2.5 keV (Fig. 8(c) and Fig. 8(d)), the photons flux of the beamline at this station is above 7×10^{10} photons/s@2.5keV.

µXAS and µXANES detection can be done in the SKB vessel, too. A one-channel SDD (Vortex, Hitachi USA) with a collimated active area of $50\ \mathrm{mm}^2$ is installed perpendicularly to the beamline for µXRF and PFY detection. Different from the microprobe end-station, a Be window (8 µm thickness) is used to separate the vacuum of mirrors and samples. Thus, micro X-ray fluorescence (µXRF) and micro X-ray absorption near-edge structure (µXANES) under vacuum or He atmosphere can be achieved at the sub-microprobe end-station.

IV. SUMMARY

The tender energy spectroscopy beamline at SSRF has been constructed completely and opened to users since Jan. 2024. Photon energy between 2.1-16 keV with resolution below 1.64×10^{-4} ($\Delta\mathrm{E}/\mathrm{E}$@2.5 keV) has been obtained at the beamline. XAS spectrum done by transmission, PFY, TEY and TFY modes have been opened to users with a spot size of $\sim 670 \times 710\ \mu\mathrm{m}^2$ under vacuum or He atmosphere. Based on two sets of Kirkpatrick–Baez mirrors systems, a spot size of nearly $\sim 3.3 \times 1.3\ \mu\mathrm{m}^2$ with the photons flux of 2.48×10^{12} photons/s@10keV and a smaller spot size of $\sim\ 0.5 \times 0.25\ \mu\mathrm{m}^2$ with the photons flux of 7×10^{10} photons/s@2.5keV have been obtained on the microprobe and sub-microprobe end-stations. Micro X-ray fluorescence (µXRF), and micro X-ray absorption near-edge structure (µXANES) will be opened to users in the near future.

[1] J. H. He, Z. T. Zhao, Shanghai synchrotron radiation facility, National Science Review **1**, 171-172 (2014). doi: 10.1093/nsr/nwt039

[2] M. H. Jiang, X. Yang, H. J. Xu et al. Shanghai Synchrotron Radiation Facility. Chin. Sci. Bull. **54**, 4171–4181 (2009). doi:10.1007/s11434-009-0689-y

[3] R. Z. Tai, Z. T. Zhao, Overview of SSRF phase-II beamlines. NUCL SCI TECH, **35**, 137 (2024). doi:10.1007/s41365-024-01487-1

[4] L. X. Yin, R. Z. Tai, D. Wang et al., Progress and future of shanghai synchrotron radiation facility. J. Vac. Soc. Jpn. **59**, 198–204 (2016). doi:10.3131/jvsj2.59.198

[5] K. Yang, Z. H. Dong, C. Y. Zhou et al., Ultrahard X-ray multifunctional application beamline at the SSRF. NUCL SCI TECH **35**, 98 (2024). doi:10.1007/s41365-024-01468-4

[6] L. X. Liu, H. W. Wang, G. T. Fan et al., The SLEGS beamline of SSRF. NUCL SCI TECH **35**, 111 (2024). doi:10.1007/s41365-024-01469-3

[7] C. F. Xue, Y. Wang, Z. Guo et al., High-performance soft x-ray spectromicroscopy beamline at SSRF. Rev. Sci. Instrum. **81**, 103502 (2010). doi:10.1063/1.3491837

[8] H. S. Yu, X. J. Wei, J. Li et al., The XAFS beamline of SSRF. NUCL SCI TECH **26**, 050102 (2015). doi:10.13538/j.1001-8042/nst.26.050102

[9] L. L. Zhang, S. Yan, S. Jiang et al., Hard X-ray micro-focusing beamline at SSRF. NUCL SCI TECH **26**, 060101 (2015). doi:10.13538/j.1001-8042/nst.26.060101

[10] Y. Chen, Q. Gao, Z. Jiang et al., Quick-scanning X-ray absorption fine structure beamline at SSRF. NUCL SCI TECH **35**, 92 (2024). doi:10.1007/s41365-024-01466-6

[11] C. Gu, S. Joshi, M. H. H. Fischel et al., Saltwater intrusion increases phosphorus abundance and alters availability in coastal soils with implications for future sea level rise. Sci. Total Environ. **931**, 172624 (2024). doi: 10.1016/j.scitotenv.2024.172624]

[12] D. Hesterberg, I. McNulty, J. Thieme, Speciation of Soil Phosphorus Assessed by XANES Spectroscopy at Different Spatial Scales. J. Environ. Qual. **46**, 1190–1197, (2017). doi:10.2134/jeq2016.11.0431

[13] C. Xu, S. Wang, Z. Chen et al., Sulphur speciation and availability in long-term fertilized soil: evidence from chemical fractionation and S K-edge XANES spectroscopy. European Journal of Soil Science. **67**, 666–675 (2016). doi: 10.1111/ejss.12364

[14] J. Prietzel, A. Botzaki, N. Tyufekchieva et al., Sulfur Speciation in Soil by S K-Edge XANES Spectroscopy: Comparison of Spectral Deconvolution and Linear Combination Fitting. Environ. Sci. Technol. **45(7)**, 2878–2886 (2011). doi:10.1021/es102180a

[15] A. C. Leri, M. B. Hay, A. Lanzirotti et al., Quantitative Determination of Absolute Organohalogen Concentrations in Environmental Samples by X-ray Absorption Spectroscopy. Anal. Chem. **78(16)**, 5711–5718 (2006). doi:10.1021/ac060476m

[16] L. Monico, L. Cartechini, F. Rosi et al., Synchrotron radiation Ca K-edge 2D-XANES spectroscopy for studying the stratigraphic distribution of calcium-based consolidants applied in limestones. Sci Rep. **10**, 14337 (2020). doi:10.1038/s41598-020-71105-8

[17] W. Tan, J. R. Peralta-Videa, J. L. Gardea-Torresdey, Interaction of titanium dioxide nanoparticles with soil components and plants: current knowledge and future research needs – a critical review. Environ. Sci.: Nano **5**, 257-278 (2018). doi:/10.1039/C7EN00985B

[18] J. Diaz, E. Ingall, C. Benitez-Nelson et al., Marine Polyphosphate: A Key Player in Geologic Phosphorus Sequestration. Scinece **320**, 652-655 (2008). doi:10.1126/science.1151751

[19] J. M. Kleinsasser, B. A. Konecke, A. C. Simon et al., Sulfur speciation in dacitic melts using X-ray absorption near-edge structure spectroscopy of the S K-edge (S-XANES): Consideration of radiation-induced changes and the implications for sulfur in natural arc systems. Am. Mineral. **109(8)**, 1359-1374 (2024). doi: 10.2138/am-2022-8833

[20] A. N. Kravtsova, Synchrotron-Based X-Ray Absorption Spectroscopy for the Study of Geological Materials. J. Surf. Investig. **14**, 135–149 (2020). doi:10.1134/S1027451020020111

[21] P. Northrup, A. Leri, R. Tappero, Applications of “Tender” Energy (1-5 keV) X-ray Absorption Spectroscopy in Life Science. Protein Pept Lett. **23(3)**, 300-308 (2016). doi:10.2174/0929866523666160107114505

[22] M. Plouviez, B. Guieysse, O. Buwalda et al., Phosphorus Storage in Microalgae: STXM and XAS P K-Edge Investigation, ACS Sustainable Resour. Manage. **1(6)**, 1270–1278 (2024). 10.1021/acssusresmgt.4c00130

[23] M. Gnida, E. Y. Sneeden, J. C. Whitin et al., Sulfur X-ray Absorption Spectroscopy of Living Mammalian Cells: An Enabling Tool for Sulfur Metabolomics. In Situ Observation of Uptake of Taurine into MDCK Cells. Biochemistry **46(51)**, 14735–14741 (2007). doi: 10.1021/bi701979h

[24] T. Wang, T. Q. Zhu, Z. Y. Feng et al., Synchrotron radiation-based multi-analytical approach for studying underglaze color: The microstructure of Chinese Qinghua blue decors (Ming dynasty). Anal. Chim. Acta. **928**, 20–31 (2016). 10.1016/j.aca.2016.04.053

[25] W. Xu, S. Lang, K. Wang et al., Fundamental mechanistic insights into the catalytic reactions of Li-S redox by Co single-atom electrocatalysts via operando methods. Sci. Adv. **9**, eadi5108 (2023). doi:10.1126/sciadv.adi5108

[26] X. J. Zhu, Q. S. Guo, Y. F. Sun et al., Optimising surface d charge of AuPd nanoalloy catalysts for enhanced catalytic activity, Nat Commun. **10(1)**, 1428, (2019). doi: 10.1038/s41467-019-09421-5.

[27] V. A. Schoepfer, M. B. J. Lindsay, X-ray absorption spectroscopy and X-ray diffraction data for molybdenum minerals and compounds, Data in Brief **45**, 108576, (2022). doi:10.1016/j.dib.2022.108576

[28] T. R. Kulp, L. G. Miller, F. Braiotta et al., Microbiological Reduction of Sb(V) in Anoxic Freshwater Sediments, Environ. Sci. Technol. **48**, 218-226 (2014). doi:10.1021/es403312j

[29] J. Frederick W. Mosselmans, Paul D. Quinn et al., I18 – the microfocus spectroscopy beamline at the Diamond Light Source. J. Synchrotron Rad. **16**, 818–824 (2009). doi:10.1107/S0909049509032282

[30] M. A. Brown, A. B. Redondo, I. Jordan et al, A new endstation at the Swiss Light Source for ultraviolet photoelectron spectroscopy, X-ray photoelectron spectroscopy, and X-ray absorption spectroscopy measurements of liquid solutions. Rev. Sci. Instrum. **84**, 073904 (2013). doi:10.1063/1.4812786

[31] Q. Xiao, A. Maclennan, Y. Hu et al., Medium-energy microprobe station at the SXRMB of the CLS. J. Synchrotron Rad. **24**, 333-337 (2017). doi:10.1107/S1600577516017604

[32] M. Cotte, E. Pouyet, M. Salomé, The ID21 X-ray and infrared microscopy beamline at the ESRF: status and recent applications to artistic materials. J. Anal. At. Spectrom. **32**, 477-493 (2017). doi: 10.1039/c6ja00356g

[33] P. Northrup, The TES beamline (8-BM) at NSLS-II: tender-energy spatially resolved X-ray absorption spectroscopy and X-ray fluorescence imaging. J. Synchrotron Rad. **26**, 2064-2074 (2019). doi:10.1107/S1600577519012761

[34] H. Ohashi, E. Ishiguro, Y. Tamenori et al., Outline of soft X-ray photochemistry beamline BL27SU of SPring-8. Nucl. Instrum. Methods Phys. Res. A, **467-468**, 529–532 (2001). doi:10.1016/S0168-9002(01)00404-1

[35] L. Zheng, Y. D. Zhao, K. Tang et al., A new experiment station on beamline 4B7A at Beijing Synchrotron Radiation Facility. Spectrochimica Acta Part B: Atomic Spectroscopy **101**, 1–5, (2014). doi:10.1016/j.sab.2014.07.006

[36] D. G. Liu, M. H. Lee, Y. J. Lu et al., Design of Tender X-ray Absorption Spectroscopy Beamline in Taiwan Photon Source,

J. Phys.: Conf. Ser. **2380**, 012041, (2022). doi:10.1088/1742-6596/2380/1/012041

[37] H. Xie, G. Du, K. Li et al., Development of fast x-ray imaging beamline at SSRF. Proc. SPIE. **12169**, 121693B (2022). doi:10.1117/12.2623647

[38] K. Li, H. L. Xie, Y. N. Fu et al., Fast X-ray imaging beamline at SSRF. NUCL SCI TECH **35**, 154 (2024). doi:10.1007/s41365-024-01488-0

[39] N-E Sung, I-J Lee, S-h Jeong et al., Characteristics of a tapered undulator for the X-ray absorption fine-structure technique at PLS-II, J. Synchrotron Rad. **21**, 1282–1287 (2014). doi:10.1107/S1600577514015549

[40] Z. Q. Jiang, H. W. Du, C. Chen et al., Supporting and driving system for in-vacuum undulator, NUCL SCI TECH **22**, 1-4 (2011). doi:10.13538/j.1001-8042/nst.22.1-4

[41] ID21 Phosphorus XANES spectra database. https://www.esrf.fr/files/live/sites/www/files/UsersAndScience/Experiments/XNP/ID21/phosphorous/Inorganic %20$Compounds/Monopotassium_phosphate.pdf$

[42] W. R. Bower, K. Morris, J. F. W. Mosselmans et al., Characterising legacy spent nuclear fuel pond materials using microfocus X-ray absorption spectroscopy, Journal of Hazardous Materials, **317**, 97-107 (2016). doi:10.1016/j.jhazmat.2016.05.037

[43] ID21 Sulfur XANES spectra database home. https://www.esrf.fr/files/live/sites/www/files/UsersAndScience/Experiments/XNP/ID21/php/gypsum/gypsum.pdf

[44] Reference X-ray Spectra of Metal Foils. Reference X-ray Spectra of Metal Foils

[45] S. Khalid, W. Caliebe, P. Siddons et al., Quick extended x-ray absorption fine structure instrument with millisecond time scale, optimized for in situ applications, Review of Scientific Instruments **81**, 015105 (2010). doi:10.1063/1.3276679

[46] C-W. Pao, J-L. Chen, J-Fu. Lee et al., The new X-ray absorption fine-structure beamline with sub-second time resolution at the Taiwan Photon Source, J. Synchrotron Rad. **28**, 930–938 (2021). doi:10.1107/S1600577521001740

[47] K. Schneider, D. Zajac, M. Sikora et al., XAS study of TiO_2-based nanomaterials, Radiation Physics and Chemistry **112**, 195-198 (2015). doi:10.1016/j.radphyschem.2015.03.010

[48] G. Dalba, P. Fornasini, Y. Soldo et al., PIN Silicon Diodes as EXAFS Signal Detectors, J. Synchrotron Rad. **3**, 213-219 (1996). doi: 10.1107/S0909049596006073

[49] Y. Li, L. Guo, M. Du et al., Unraveling distinct effects between CuOx and PtCu alloy sites in Pt-Cu bimetallic catalysts for CO oxidation at different temperatures. Nat. Commun., **15**, 5598 (2024). doi:10.1038/s41467-024-49968-6

[50] K. Yan, X. Ge, W. Li et al., Regulation of a Ni_3Sn_2 intermetallic catalyst using highly dispersed Pd species to boost propyne semihydrogenation. J. Mater. Chem. A, **12**, 16482–16490 (2024). doi:10.1039/d4ta02342k

[51] M. Lin, R. Qi, W. Zhang et al., Unravelling Ultra-Stable Conversion-Type Zinc-Ion Storage in Copper Selenides for Flexible Aqueous Batteries. Adv. Energy Mater., **14**, 2401288 (2024). doi:10.1002/aenm.202401288.

[52] H. Ando, M. Horio, Y. Takeo et al., Developing a Simple Scanning Probe System for Soft X-ray Spectroscopy with a Nano-focusing Mirror, e-Journal of Surface Science and Nanotechnology, **21**, 200-206 (2023). doi:10.1380/ejssnt.2023-020